Journal of Molecular Graphics and Modelling 51 (2014) 149–157

Contents lists available at ScienceDirect

Journal of Molecular Graphics and Modelling

journal homepage: www.elsevier.com/locate/JMGM

Theoretical characterization and design of highly efficient iridium (III) complexes bearing guanidinate ancillary ligand

Xin-Yao Ren, Yong Wu, Li Wang, Liang Zhao, Min Zhang*, Yun Geng*, Zhong-Min Su**

Institute of Functional Material Chemistry, Faculty of Chemistry, Northeast Normal University, Changchun 130024, People's Republic of China

ARTICLE INFO

Article history:
Accepted 17 May 2014
Available online 27 May 2014

Keywords:
Iridium
Guanidinate
Phosphorescence
OLED
Spin-orbital coupling
DFT

ABSTRACT

A density functional theory/time-depended density functional theory was used to investigate the synthesized guanidinate-based iridium(III) complex [$(ppy)_2Ir\{(N^iPr)_2C(NPh_2)\}$] (**1**) and two designed derivatives (**2** and **3**) to determine the influences of different cyclometalated ligands on photophysical properties. Except the conventional discussions on geometric relaxations, absorption and emission properties, many relevant parameters, including spin-orbital coupling (SOC) matrix elements, zero-field-splitting parameters, radiative rate constants (k_r) and so on were quantitatively evaluated. The results reveal that the replacement of the pyridine ring in the 2-phenylpyridine ligand with different diazole rings cannot only enlarge the frontier molecular orbital energy gaps, resulting in a blue-shift of the absorption spectra for **2** and **3**, but also enhance the absorption intensity of **3** in the lower-energy region. Furthermore, it is intriguing to note that the photoluminescence quantum efficiency (Φ_{PL}) of **3** is significantly higher than that of **1**. This can be explained by its large SOC value $<T_1|H_{SO}|S_n>$ ($n = 3$–4) and large transition electric dipole moment (μ_{S3}), which could significantly contribute to a larger k_r. Besides, compared with **1**, the higher emitting energy (E_{T1}) and smaller $<S_0|H_{SO}|T_1>^2$ value for **3** may lead to a smaller non-radiative decay rate. Additionally, the detailed results also indicate that compared to **1** with pyridine ring, **3** with imidazole ring performs a better hole injection ability. Therefore, the designed complex **3** can be expected as a promising candidate for highly efficient guanidinate-based phosphorescence emitter for OLEDs applications.

1. Introduction

Phosphorescent organic light-emitting diodes (PhOLEDs) based on heavy transition-metal complexes have fueled tremendous attention due to their higher efficiencies than those of fluorescent emitters [1–3]. Extensive research has been carried out to promote PhOLEDs into commercial applications as full-color flat-panel displays and solid-state lighting resources [4–6]. Thus, the selection of a proper metal-based phosphorescent material is of great pivotal to obtain highly efficient electroluminescence for PhOLEDs.

Cyclometalated complexes containing iridium(III) metal center have been extensively studied and widely used in OLEDs as the phosphors because of their unique photophysical properties. These Ir(III) metal ions prefer a six-fold coordination that can be described as an octahedral symmetry, and thus the magnitude of d-orbital splitting is large [7,8]. More importantly, cyclometalated Ir(III) complexes have strong spin-orbit coupling (SOC) effects, which facilitate the intersystem crossing (ISC) from singlet to triplet states and result in efficient population of the lowest lying triplet state. [9]. Furthermore, by modifying the ligand structure and/or incorporation of ancillary ligands, these cyclometalated iridium(III) complexes can realize emission in the full visible spectra [10]. As a result, owning to their superior features, these Ir^{3+} complexes are regarded as promising candidates of phosphorescent emitters for high-performance OLEDs [11].

Compared with homoleptic complexes $Ir(C\hat{N})_3$, heteroleptic iridium(III) complexes $(C\hat{N})_2Ir(LX)$, comprising two cyclometalated ($C\hat{N}$) main ligands and a bidentate ancillary ligand (LX), are more promising phosphorescent emitters, because of their easy synthetic chemical accessibility, flexibility in emission energy and efficiency tuning [12]. For example, a well-known green phosphorescent dopant, $Ir(ppy)_2(acac)$ (acac = acetylacetonate, ppy = 2-phenylpyridine) was reported by Yang and Ma et al. with a high external quantum efficiency (EQE) of 23.7% and a maximum power efficiency ($\eta_{p,max}$) of 105 lm/W [13,14]. In addition, on the basis of this phosphorescent dye, a sky-blue emitter of Ir(III)

* Corresponding authors.
** Corresponding author. Tel: +86-0431-85099108; fax: +86-431-85684009.
E-mail addresses: zhangm914@nenu.edu.cn (M. Zhang), gengy575@nenu.edu.cn (Y. Geng), zmsu@nenu.edu.cn, zmsu@hotmail.com (Z.-M. Su).

http://dx.doi.org/10.1016/j.jmgm.2014.05.005
1093-3263/

phosphor named FIrpic, was designed by fluorine atom modified phenyl ring in ppy and altering the ancillary ligand with pic (picolinate) [15,16]. As for iridium(III) complexes, the ancillary ligands were in most of the cases acac, pic or their derivatives and often combined with CN̂ ligands such as ppy, since the emitting lights of these series of complexes can be tuned flexibly.[17] However, these Ir(III)-based doped devices may exhibit significant efficiency roll-off upon increasing brightness and current density, due to triplet–triplet annihilation (TTA), for instance $[(C\hat{N})_2Ir(acac)]$ complexes based devices [18–20]. Such passive electroluminescence (EL) performance promotes us to search for highly efficient iridium(III) complexes with appropriate ancillary ligands.

Monoanionic guanidinate groups $[(N^iPr)_2C(NR^1R^2)]^-$, as an alternative to cyclopentadienyl-based ligands, have been increasingly used in organometallic chemistry [21]. These guanidinate ligands have the advantages of tunable electronic and steric effects by variation of the substituents on the nitrogen atoms and flexible coordination modes [22–26]. Despite the various transition-metal guanidinates reported to date, iridium(III) complexes bearing ancillary guanidinate ligands are still limited [23,27,28]. Only recently, guanidinate groups were firstly reported by Hou and co-workers as ancillary ligands for the phosphorescent iridium(III) complexes [29]. A series of luminescent heteroleptic bis(pyridylphenyl) iridium(III) complexes with various ancillary guanidinate ligands $[(ppy)_2Ir\{(N^iPr)_2C(NR_2)\}]$ have been synthesized [29]. Among these complexes, they find that $[(ppy)_2Ir\{(N^iPr)_2C(NPh_2)\}]$ (**1**) (Fig. 1) whose ancillary ligand is derived from the diphenylamino-substituted guanidinate ligand shows better EL efficiencies accompanied by little efficiency roll-off at high luminance [30]. These results should be attributed to its steric hindrance of the diphenylamino-substituted guanidinate ligand in the periphery of the iridium metal, which results in a twisted conformation and prevents intermolecular interaction, thus reducing the self-quenching and TTA process at high currents [29,30]. Moreover, triphenylamine possesses a higher hole mobility and excellent hole transport ability. Hence, incorporate its branched diphenylamino to the guanidinate ancillary ligand could stabilize electron-deficient metal center and improve the hole-injection (HI) and hole-transport (HT) abilities of the resulting complex [29]. Consequently, this complex $[(ppy)_2Ir\{(N^iPr)_2C(NPh_2)\}]$ (**1**) may serves as a bifunctional phosphorescent emitter.

However, according to the experimental values, the nonradiative decay rate constant (k_{nr}) is nearly two times larger than the radiative rate constants (k_r) of **1**, which may hamper its development of better OLED devices. In this manuscript, considering the advantages of this type of ancillary ligand, we designed two derivatives on the basis of **1** by modifying the pyridyl functionality of ppy with diazole as main ligand (complexes **2** and **3** in Fig. 1) with the hope of enhancing phosphorescence efficiency. Systematical density functional theory/time-depended density functional theory (DFT/TD-DFT) calculations were performed on **1**–**3** to gain a deeper insight into their geometric relaxations, electronic structures, spectral properties, phosphorescence efficiencies and to explore the influences of different diazole ligands on these photophysical properties. Importantly, to find the detailed origin of phosphorescence efficiency, many relevant parameters including SOC matrix elements, Zero-field-splitting (ZFS) parameters, radiative rate constants (k_r) and so on were quantitatively evaluated, which deepens our understanding at the same time. Moreover, the performance of HI and balanced charge transfer properties of OLED device based on these complexes, which is judged by ionization potentials, and the reorganization energies have also been studied. Finally, we hope this work can theoretically select highly efficient guanidinate ligated iridium(III) complexes for OLED.

2. Computational details

In this work, restricted and unrestricted [31] formalisms were adopted respectively in the ground-state (S_0) and the lowest triplet state (T_1) geometries optimization by using the DFT [32] calculations with PBE0 and UPBE0 exchange-correlation functional [31,33] without symmetry constrains. All the complexes were optimized in the gas phase. Vibrational frequencies for these studied complexes were performed at the same level to ensure that each of the optimized geometry is a minimum on the potential energy surface. On the basis of the equilibrium S_0 and T_1 geometries, the TD-DFT calculations [34–36] were also applied to investigate the absorption and $T_1 \rightarrow S_0$ emission spectral properties for these studied systems at the same level. Solvent effect in dichloromethane (CH_2Cl_2) was also taken into account using the polarized continuum model (PCM) [37] approach to model a valid approximation of chemical environment.

In terms of basis set, the Hay-Wadt effective core potential (ECP) and a double-ζ basis set LANL2DZ [38] was employed for iridium atom and 6-31G(d,p) for nonmetal atoms. To demonstrate the accuracy of PBE0 functional with LANL2DZ ECP basis set, different functional levels and basis sets for **1** have been tested and the obtained results are listed in Table S1 with experimentally detected geometry data in hand. It is found that the level of theory PBE0/LANL2DZ/6-31G(d,p) can give an optimal structure, and small deviations in geometrical parameters between experimental and theoretical results are reasonable and acceptable. Meanwhile, to choose a suitable functional for TD-DFT calculation, different functional methods (PBE0, B3LYP, M052X and M062X) in solution with same basis set LANL2DZ/6-31G(d,p) were employed to predict emission spectra of **1**. The corresponding results are listed in Table S2 with experimental value. It indicates that the PBE0 functional is more reliable to reproduce the experimental datum. Therefore, the PBE0 functional is appropriate for TD-DFT calculations to predict the spectral properties of Ir(III) complexes.

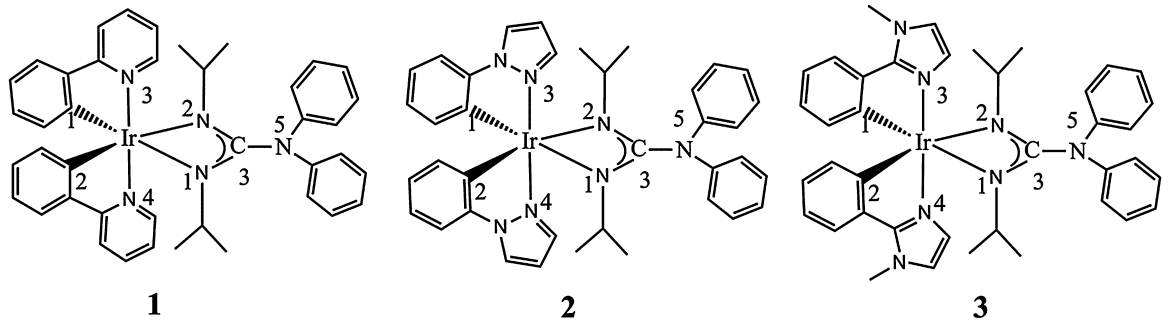

Fig. 1. Molecular structures of the investigated complexes **1**–**3**.

Table 1
Selected bond lengths (Å) and angles (°) for the studied complexes in the ground (S_0) and the lowest-lying triplet (T_1) states at the PBE0/LANL2DZ level.

Parameter	1		2		3	
	S_0	$T_1(\Delta_{T_1-S_0})$[a]	S_0	$T_1(\Delta_{T_1-S_0})$[a]	S_0	$T_1(\Delta_{T_1-S_0})$[a]
Ir-C1	2.000	1.975(−0.025)	2.011	1.963(−0.048)	2.013	1.987(−0.026)
Ir-C2	2.000	1.975(−0.025)	2.011	2.003(−0.008)	2.013	2.013(0)
Ir-N1	2.219	2.233(0.014)	2.196	2.214(0.018)	2.203	2.221(0.018)
Ir-N2	2.219	2.233(0.014)	2.196	2.210(0.014)	2.203	2.200(−0.003)
Ir-N3	2.040	2.040(0)	2.017	2.015(−0.002)	2.030	1.995(−0.035)
Ir-N4	2.040	2.040(0)	2.017	2.028(0.011)	2.030	2.041(0.011)
N1-Ir-N2	59.8	59.2(−0.6)	60.3	59.8(−0.5)	60.1	59.9(−0.2)
C1-Ir-N4	94.9	94.5(−0.4)	95.3	95.1(−0.2)	95.1	94.2(−0.9)
N3-Ir-N4	173.4	174.3(0.9)	173.4	174.4(1.0)	172.8	173.0(0.2)

[a] The geometric differences between S_0 and T_1 states.

Aforementioned calculations on electronic singlet and triplet states of studied complexes have been performed with the Gaussian 09 program package [39]. In addition, the perturbative spin-orbit zeroth-order regular approximation (ZORA) [40,41] TD-DFT method with the statistical average of orbital potentials (SAOP) as well as all electron TZ2P basis set was carried out to evaluate the photoluminescence quantum efficiency (Φ_{PL}) by using the Amsterdam Density Functional (ADF2013.01) program package [42]. The relativistic effects were also taken into account in the TD-DFT calculations. Therefore, the k_r, SOC values, ZFS parameters, metal-based charge transfer character (^{3}MLCT%) were calculated based on the optimized lowest triplet excited-state geometry. What's more, AOMix program [43] was employed for measuring molecular orbital compositions and GaussSum 2.2 program [44] for absorption spectra analysis.

3. Results and discussion

3.1. Molecular geometries in the ground and the lowest triplet excited state

Structural drawings of the investigated complexes **1**–**3** are depicted in Fig. 1, along with the numbering of some key atoms, and the optimized ground-state geometrical structures of them are presented in the Supporting Information (Fig. S1). To gain a better understanding of geometry relaxation from S_0 to T_1 state, the main optimized geometry parameters for the S_0 and T_1 states of **1**–**3** are given in Table 1.

As depicted in Fig. S1, the three complexes in the S_0 state possess a slightly distorted octahedral geometry with two CN̂ ligands and one guanidinate ligand [$(N^iPr)_2C(NPh_2)$] surrounding the iridium metal center. The four core atoms N1, N2, N5 and C3 of the guanidinate unit and the central Ir(III) atom in **1**–**3** are placed in a nearly square plane, which is in line with those analogous [$(CN̂)_2Ir\{(N^iPr)_2C(NPh_2)\}$] complexes as synthesized by Hou and co-workers [30].

According to Table 1, the geometry parameters in S_0 state indicate that the alteration of ppy main ligand can change the metal-ligand bond lengths to some extent. For the designed complex **2** (**3**), the Ir—N1 and Ir—N2 bond lengths are shortened by 0.023 and 0.023 Å (0.016/0.016 Å) compared with those of **1**. Meanwhile, same situation can also be observed for Ir—N3 and Ir—N4 distances for **2** and **3**. These features indicate the strong coordination interaction between the Ir(III) center and ligands for **2** and **3**, which may promote their charge transfer transition from metal to ligands. Moreover, it is noted that both in S_0 and T_1 states, the Ir—N1 and Ir—N2 bond lengths are apparently larger than the rest of the metal-ligand bonds for **1**–**3**, which can be interpreted as a consequence of the steric hindrance of the guanidinate ligand. In contrast to complex **2** with pyrazole ligand, the Ir—N3 and Ir—N4 bond lengths in **3** with imidazole ligand are elongated (both are 0.013 Å), which is attributed to the different positions of nitrogen (N) atom. Besides, in comparison with metal-ligand bond distance, a negligible variation of bond angle (less than 1.4°) can be observed among the three complexes.

From the S_0 to T_1 state, there are no significant changes for metal-ligand bond distances with a small difference within 0.02 Å, except for Ir—C1 in **1**–**3** (Table 1). Compared with the case in S_0 state, the Ir—C1 bond lengths in T_1 state for the three complexes are reduced by 0.025, 0.048 and 0.026 Å respectively, which would suggest that the phenyl ligand of CN̂ moiety is most involved in the excited states. For the studied complexes, slightly elongated Ir—N1 and Ir—N2 bonds are observed in T_1 state, which can be explained by negligible electron density distributions of guanidinate ancillary ligand to the LUMOs in Fig. 2. For Ir—N3 bond length, it is drastically shortened by 0.035 Å in the T_1 state of complex **3**, leading to an enhanced interaction between iridium and imidazole of the cyclometalated ligand. It is worth noting that the changes of bond angle for the three complexes are minor (less than 1°) upon $S_0 \rightarrow T_1$ excitation. To sum up, the geometry relaxation for complexes **1**–**3** from S_0 to T_1 state is comparative.

3.2. Frontier molecular orbital properties in the ground state

To probe into the effects of CN̂ ligands on optoelectronic properties, the calculated frontier orbital energy gaps, energy levels and orbital distribution of the complexes in the ground state will be discussed in detail. For comparison, the calculated HOMO to HOMO − 1 and LUMO to LUMO + 1 energy levels and orbital compositions are presented in Fig. 2 and Table 2. Furthermore, the detailed descriptions of FMOs for the relevant complexes are listed Table S3.

As can be seen from Table 2, the HOMO of complex **1** consists principally of Ir (t_{2g}) orbital (32.88%) in antibonding combination with the π orbitals of the guanidinate ancillary ligand [$(N^iPr)_2C(NPh_2)$] (39.70%) and phenyl rings of CN̂ ligands, while the LUMO is localized almost exclusively (94.59%) on the CN̂ ligands, as evident from the electron density distributions presented in Fig. 2. However, unlike the case of LUMOs, the electron density distributions of HOMOs for **2** and **3** are different from **1**. For complex **2**, the HOMO is predominantly located on 5d(Ir) orbital and ancillary ligand with a negligible contribution from CN̂ ligands. With respect to complex **3**, the imidazole rings of CN̂ ligands also contribute to the HOMO with a smaller proportion. This is attributed to the different positions of N atom substitution in these two complexes. When it comes to the distribution of HOMO-1, the situation for **1** is the same as HOMO, which is composed of a mixture of the Ir(III) center and the π orbitals of the guanidinate ancillary ligand and phenyl rings of CN̂ ligands. In contrast, for **2** and **3**, the contribution from the Ir(III) center and π orbitals of CN̂ ligands are obviously larger than that of HOMOs. It is noted that all the complexes possess large contribution from 5d(Ir) orbital to HOMO and HOMO-1 energy

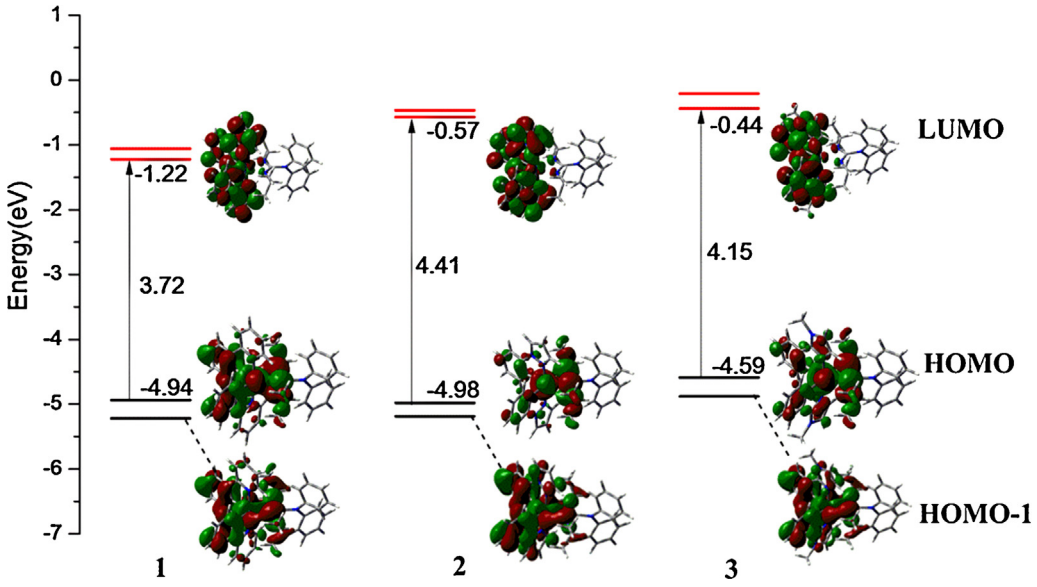

Fig. 2. Calculated energy levels, energy gaps (in eV) and electron density distribution of HOMO, HOMO-1 and LUMO for complexes **1**–**3** at their S_0 optimized geometries.

levels (especially for complex **3**), which can result in obvious MLCT characters between metal 5d(Ir) orbitals and π orbitals of ligands.

Owing to the replacement of pyridine ring with different diazole moieties, the FMOs energy levels have been markedly affected as shown in Fig. 2. As far as complex **3** is concerned, upon changing the pyrazole ring with an imidazole moiety, both the HOMO and LUMO are destabilized and the HOMO-LUMO energy gap has a 0.25 eV decrease in comparison with that of **2**. It is interesting to note that the HOMO energy of **2** is comparable with **1** (−4.98 and −4.94 eV, respectively), whereas the LUMO level is significantly destabilized due to higher energy π^* orbitals for phenylpyrazole than phenylpyridine. For **1** and **3**, the HOMO and HOMO − 1 are well separated in energy, and likewise the LUMO and LUMO + 1 energy levels. In contrast, the LUMO and LUMO + 1 of **2** are nearly degenerate orbitals. Overall, the destabilizations of the LUMOs are more markedly than those of the HOMOs for the designed complexes, which result in the enlarged HOMO–LUMO energy gaps. This can be rationalized by the fact that the contribution of the LUMO is mainly located on the CN̂ ligands.

Moreover, the energies of HOMO and LUMO are related to the hole- and electron-injection abilities [45] of these complexes. For complex **3**, the distinctly higher HOMO energy will ensure the excellent hole-injection ability compared with **1**. However, the comparative HOMO energy levels between **1** and **2** may result in the similar hole-injection ability.

3.3. Absorption spectra analysis

TD-DFT calculations with the PBE0 functional have proved its reliability to predict the low-lying singlet–singlet excited states and gain good agreement with experimental spectra of Ir(III) complexes [46,47]. In order to gain deeper insight into the electronic transition properties of the singlet–singlet excitation, the absorption process was also calculated by means of the TD-DFT/PBE0 method with PCM in dichloromethane media. The vertical transitions were calculated based on the optimized ground-state geometries. The main excited states associated with their vertical excitation energies and oscillator strengths, dominant configurations, and their

Table 2
Molecular orbital compositions (%) in the ground state for **1**–**3** at PBE0 level. (As for complex **1**, CN̂ (I) and CN̂ (II) are refer to 2-phenylpyridine ligands containing C1 and N3 atoms, C2 and N4 atoms, respectively. As for complex **2** and **3**, CN̂(I) and CN̂(II) are denoted as the phenyl-diazole ligands containing C1 and N3 atoms, C2 and N4 atoms, respectively.).

Orbital[a]	Energy (ev)	Ir	CN̂ (I)	CN̂ (II)	$(N^iPr)_2C(NPh_2)$				Characteristics
					Total	N1	N2	NPh_2	
1									
L + 1	−1.06	4.49	46.90	46.96	1.27	0.27	0.27	0.33	$\pi^*(C\hat{N})$
L	−1.22	2.54	47.33	47.26	1.49	0.39	0.39	0.34	$\pi^*(C\hat{N})$
H	−4.94	32.88	13.32	13.32	39.70	16.18	16.18	0.48	$d(Ir)+\pi(C\hat{N})/(N^iPr)_2C(NPh_2)$
H − 1	−5.22	27.42	17.05	17.06	38.00	15.17	15.18	0.47	$d(Ir)+\pi(C\hat{N})/(N^iPr)_2C(NPh_2)$
2									
L + 1	−0.47	2.42	42.39	47.88	1.39	0.22	0.22	0.59	$\pi^*(C\hat{N})$
L	−0.57	2.03	41.88	47.24	1.94	0.40	0.40	0.76	$\pi^*(C\hat{N})$
H	−4.98	23.33	5.47	5.56	65.05	26.57	26.57	0.78	$d(Ir)+\pi(N^iPr)_2C(NPh_2)$
H − 1	−5.19	34.11	22.76	24.87	15.41	5.95	5.95	0.24	$d(Ir)+\pi(C\hat{N})/(N^iPr)_2C(NPh_2)$
3									
L + 1	−0.21	2.74	47.83	47.82	1.22	0.16	0.16	0.38	$\pi^*(C\hat{N})$
L	−0.44	1.34	47.85	47.86	1.38	0.32	0.32	0.17	$\pi^*(C\hat{N})$
H	−4.59	31.47	8.33	8.33	51.30	21.02	21.02	0.59	$d(Ir)+\pi(N^iPr)_2C(NPh_2)$
H − 1	−4.88	33.36	21.69	21.69	22.31	8.82	8.82	0.27	$d(Ir)+\pi(C\hat{N})/(N^iPr)_2C(NPh_2)$

[a] H and L represent HOMO and LUMO respectively.

Table 3
Calculated wavelengths (λ_{cal}/nm), singlet excitation energies (E), oscillator strengths (f), electron transition assignments of **1**–**3** in CH_2Cl_2 media at TD-PBE0 level with experimental value.

	State	f	λ_{cal}/E (eV)	Main configurations	Assignments	Exp.[a] (nm)
1	S_1	0.0092	442(2.81)	H → L[b](96%)	MLCT/LLCT	
	S_3	0.0857	390(3.18)	H − 1 → L(96%)	MLCT/LLCT/ILCT	402
	S_8	0.0489	344(3.60)	H − 2 → L + 1(80%)	LLCT	352
	S_{34}	0.2510	263(4.71)	H − 2 → L + 6(96%)	ILCT	
	S_{36}	0.3823	259(4.78)	H − 7 → L + 1(32%)	ILCT	262
				H − 5 → L + 2(15%)	MLCT/LLCT/ILCT	
2	S_1	0.0020	356(3.49)	H → L(94%)	MLCT/LLCT	
	S_3	0.0958	329(3.76)	H − 1 → L(94%)	MLCT/LLCT/ILCT	
	S_7	0.0329	296(4.18)	H − 2 → L + 1(84%)	LLCT	
	S_9	0.0813	287(4.32)	H − 2 → L + 2(74%)	ILCT	
	S_{11}	0.2082	279(4.44)	H − 2 → L + 3(67%)	ILCT	
	S_{21}	0.1027	262(4.73)	H − 2 → L + 4(63%)	ILCT	
	S_{33}	0.1384	238(5.21)	H − 6 → L + 1(41%),	ILCT	
3	S_1	0.0140	383(3.24)	H → L (95%)	MLCT/LLCT	
	S_3	0.1033	345(3.60)	H − 1 → L(95%)	MLCT/LLCT/ILCT	
	S_9	0.0862	291(4.26)	H − 2 → L + 2(72%)	MLCT/ILCT	
	S_{14}	0.1277	283(4.39)	H − 2 → L + 3(56%)	MLCT/ILCT	
	S_{15}	0.1156	280(4.42)	H → L + 6(43%)	MLCT/LLCT	
	S_{24}	0.2221	259(4.79)	H − 2 → L + 5(80%)	MLCT/ILCT	
	S_{32}	0.3256	251(4.95)	H − 6 → L(69%)	MLCT/ILCT	

[a] Ref. [29].
[b] H and L represent HOMO and LUMO respectively.

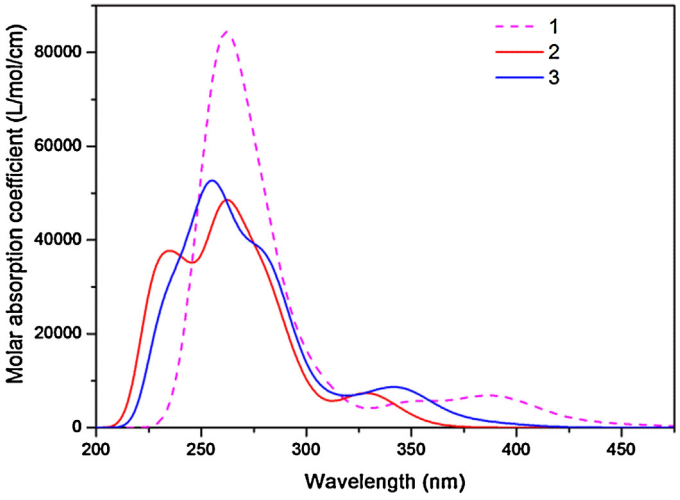

Fig. 3. Simulated absorption spectra of **1**–**3** in CH_2Cl_2 media.

corresponding assignments are summarized in Table 3, along with the experimental data for **1**. Simulated absorption spectra of **1**–**3** are displayed in Fig. 3. The calculated maximum absorption peak for **1** (259 nm) corresponds well to experimental value (262 nm) with a small deviation of 3 nm at higher energy [29]. Besides, the lowest-lying absorptions at 344 and 390 nm also agree with the experimental data at 352 and 402 nm for **1** [29], confirming the reliability of this level of theory.

It can be seen in Fig. 3, the calculated absorption spectra of **1**–**3** display two distinct absorption regions, however, the position and intensity of absorption peaks are different. In the case of complexes **1** and **2**, the simulated absorption spectra show intense features in the ultraviolet region below 300 nm with maxima at 259 and 279 nm, respectively. For **1**, the intense absorption band can be described as the spin-allowed ^{1}LLCT (ligand to ligand charge transfer) and ^{1}ILCT (intraligand charge transfer) $^1\pi\pi^*$ transitions and ^{1}MLCT (metal to ligand charge transfer) characters. However, for **2**, this strongest absorption band is characterized as ^{1}ILCT transition involving guanidinate ligand. In comparison with **2**, the calculated intense absorption peak at 251 nm of **3** is obviously blue-shifted (28 nm) and can be defined as a mixture of ^{1}MLCT and ^{1}ILCT transitions. Besides, the oscillator strength for **3** is relatively higher than **2** at the maximum absorption peak, indicating the different substituent effects of nitrogen (N) atom. For the three complexes, the lowest absorption ($S_0 \rightarrow S_1$) energies are in the following order (Table 3): **2** > **3** > **1**, which are in line with the variation trend of HOMO–LUMO energy gaps. According to Table 3, such lowest-lying excitation can be assigned as charge transfer transitions with ^{1}MLCT and ^{1}LLCT characters. As shown in Fig. 3 and Table 3, the weaker and lower-energy bands of **1** (325–450 nm) are mainly ruled by S_1 (HOMO → LUMO), S_3 (HOMO − 1 → LUMO) and S_8 (HOMO − 2 → LUMO + 1) excited states that are described predominantly as ^{1}MLCT, ^{1}LLCT, and overlap with a certain amount of ^{1}ILCT transitions. However, compared with **1**, the less intense bands of **2** and **3** are obviously blue shift in the range of 320–400 nm with the same transition assignments, which are also corresponding to the mixed ^{1}MLCT, ^{1}LLCT and ^{1}ILCT transitions. What's more, owing to the replacement of pyridine ring in the ppy with imidazole ligand, the more intense absorption for **3** relative to **1** and **2** in the lower-energy region can be observed, which would enhance the ISC process between singlet and triplet states. As above-mentioned, we can conclude that the variation of CN̂ ligand has been demonstrated as an effective strategy to tune the photophysical properties of these studied Ir(III) complexes.

3.4. Phosphorescence properties

To further investigate the nature of the lowest-lying emission transitions for the studied complexes, the phosphorescent emission energies at their optimized T_1 geometries were calculated with the same level (denoted as TD-PBE0/LANL2DZ/6-31G(d,p)). The calculated results are reported in Table 4, along with the corresponding experiment data. In addition, the molecular orbital compositions in the lowest triplet states are collected in Table S4.

As shown in Table 4, the calculated vertical $T_1 \rightarrow S_0$ emission at 559 nm for complex **1** matches well with the experimental value of 535 nm. Compared with **1**, a remarkable blue shift is detected for **2**, which can be ascribed to the higher triplet energy for pyrazole than that of pyridine [48], while a comparable emission wavelength has been observed for **3**. Such different situation on the emission wavelengths for **2** and **3** is originated from the

Table 4
The calculated emission wavelength (λ_{cal}/nm), the main transition configurations and assignments of **1**–**3** in CH_2Cl_2 solution at TD-PBE0 level with experimental value.

	State	λ_{cal}	Configurations	Assignments	Exp. (nm)
1	T_1	559	H → L[b](85%)	^{3}MLCT/^{3}LLCT/^{3}ILCT	535[a]
2	T_1	505	H → L(59%)	^{3}MLCT/^{3}LLCT/^{3}ILCT	
			H − 1 → L(17%)	^{3}MLCT/^{3}LLCT/^{3}ILCT	
3	T_1	567	H → L(52%)	^{3}MLCT/^{3}LLCT/^{3}ILCT	
			H − 1 → L(17%)	^{3}MLCT/^{3}LLCT/^{3}ILCT	

[a] Ref. [29].
[b] H and L represent HOMO and LUMO respectively.

different substituted N atom positions on the main ligands. As can be seen from Table 4, T_1 states for **2** and **3** are described in terms of linear combination of HOMO → LUMO and HOMO − 1 → LUMO. As far as complex **1** is concerned, the calculated lowest-energy emission is mainly from HOMO → LUMO (85%). According to Table S4, the HOMO of **1** delocalizes mainly on the 5d(Ir) orbital (33.82%) and π orbitals of both the CN̂ (I) and CN̂ (II) ligands (21.65% and 21.65%), being mixed with an amount of ancillary ligand (21.9%), while LUMO primarily resides on the π^* orbitals of the CN̂ (I) and CN̂ (II) moieties. Therefore, the observed emission of **1** can be assigned to $^3M_{d\pi}L_{\pi^*(C\hat{N})}CT/^3L_{\pi(NiPr)2C(NPh2)}L_{\pi^*(C\hat{N})}CT/^3I_{\pi(C\hat{N})}L_{\pi^*(C\hat{N})}CT$ characters. When it comes to complexes **2** and **3**, the mixed transitions of HOMO → LUMO and HOMO − 1 → LUMO are contributing to their T_1 states, which can be reasonably described as $^3M_{d\pi}L_{\pi^*(C\hat{N})}CT/^3L_{\pi((NiPr)2C(NPh2)}L_{\pi^*(C\hat{N})}CT/^3I_{\pi(C\hat{N})}L_{\pi^*(C\hat{N})}CT$ mixed characters. Besides, these results are also in agreement with the analysis of the T_1 geometry structure as we mentioned above. In the case of complexes **2** and **3**, the enhanced interaction between metal and CN̂ ligands may be ascribed to the decreased Ir—C1 and Ir—N3 bond lengths. Moreover, the corresponding nature of the emitting excited state (T_1) for the three complexes can also be rationalized by the total electron density difference at their T_1 optimized geometry as depicted in Fig. 4. For the complex **3**, in addition to the guanidinate of the ancillary ligand [$(N^iPr)_2C(NPh_2)$], the diphenylamino with better electron-donating ability also takes part in the charge transfer transitions. It is noteworthy that the contributions of 5d(Ir) orbital in the occupied orbitals (especially HOMOs) for the three complexes are large (Table S4), resulting in a significant ^{3}MLCT participation and hence benefit a high Φ_{PL}.

3.5. Theoretical prediction of quantum yield

According to the Kasha rule, TD-DFT approach with SOC effects was employed at the optimized T_1 geometry to obtain SOC matrix elements, k_r, and ZFS parameters for the three complexes. Theoretically, the quantum yield Φ_{PL} can be defined as follows:

$$\Phi_{PL} = \frac{k_r}{k_r + k_{nr}} \quad (1)$$

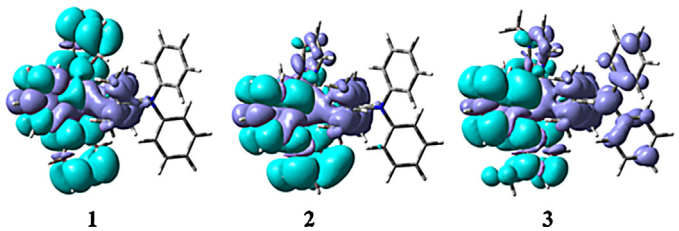

Fig. 4. Total electron density difference map for **1**–**3** at their T_1 geometry. Purple and turquoise colors show regions of decrease and increase in electron density, respectively. (For interpretation of the references to color in this figure legend, the reader is referred to the web version of the article.)

Table 5
SOC matrix elements (cm^{-1}) of **1**–**3** at their respective T_1^{opt} optimized geometries obtained by the ADF2013.01 program package.

	S_1	S_2	S_3	S_4	S_5	S_6
1						
T_1	41.6	26.3	253	293	15.9	8.17
T_2	26.5	48.2	36.0	55.1	51.7	229
T_3	274	6.48	57.2	229	8.97	26.2
T_4	324	101	273	3.21	16.8	30.8
2						
T_1	140	197	160	229	26.7	7.6
T_2	256	149	129	175	38.1	4.37
T_3	21.2	29.7	74.9	59.8	268	11.5
T_4	276	207	163	77.4	43.5	4.79
3						
T_1	71.1	64.4	392	411	15.1	8.02
T_2	331	29.9	125	297	17.0	3.06
T_3	131	41.5	83.6	62.2	17.5	5.99
T_4	459	72.3	394	68.3	12.9	2.10

Therefore, larger k_r and smaller k_{nr} are desired for a high quantum yield. Theoretically, k_r is related to the SOC matrix elements between triplet and singlet manifolds, the transition dipole moment ($\langle S_n|M|S_0\rangle$) between the n_{th} singlet excited state (S_n) and the singlet ground state (S_0), energy gap between S_n and T_m, and $E(T_m)$ represents the energy of the $T_m \rightarrow S_0$ transition [49,50]. The equation is expressed as:

$$k_r(T_m \rightarrow S_0) \approx \frac{16\pi^3 10^6 n^3 E(T_m)^3}{3h\varepsilon_0} \left\{ \sum_n \frac{\langle \psi_{T_m}|H_{SO}|\psi_{S_n}\rangle}{E(S_n) - E(T_m)} \langle S_n|M|S_0\rangle \right\}^2 \quad (2)$$

where n, h and ε_0 are the refractive index of the medium, Planck's constant, and the permittivity in vacuum, respectively.

Previous works have corroborated that the SOC effects in theoretical calculations can provide a reliable way to elucidate ISC among different spin multiplicities as well as the k_r value of phosphorescent process [11,51]. Hence, the SOC matrix elements between low-lying singlet and triplet states were calculated through the TD-DFT method, and the results are given in Table 5.

As illustrated by the calculated results in Table 5, the SOC matrix elements don't exhibit a law overall. However, quantitative comparison can be made according to the different excited states. As far as S_3 state is concerned, which possesses large oscillator strength for the absorption in **1**–**3**, the SOC matrix elements $\langle T_m|H_{SO}|S_3\rangle$ for **3** are obviously larger than those of other complexes, and hence a strong mixture is therefore expected among these excited states. Meanwhile, considering the $\langle T_1|H_{SO}|S_n\rangle$ matrix elements for **1** and **3**, S_3 and S_4 excited states can have strong electronic coupling with T_1 state.

However, for complex **2**, S_1 and S_2 states can effectively couple with the T_1 state. Consequently, combining the large SOC values $\langle T_1|H_{SO}|S_n\rangle$ (n = 1–2) with small energy gaps between singlet and triplet states for **2**, a desirable ISC rate would be obtained, which is of great benefit to its higher k_r value. In addition, the contribution from $\langle T_m|H_{SO}|S_2\rangle$ matrix elements (m = 1–4) for **2** cannot be ignored, which are obviously larger than those of **1** and **3**. It should be noted that only two singlet states (S_3 and S_4) provide efficient SOC with T_1 state for **1**, which may lead to a relatively smaller k_r value from T_1 state. Therefore, it can be concluded that replacing the pyridine of ppy ligand with diazole can effectively enhance the SOC process, which is beneficial to increase the k_r. It is well known that increasing contributions from d orbitals of metal ion in the singlet–triplet transition, lead to an enhanced percentage of ^{3}MLCT characters, and thus contribute to the first-order SOC values [52]. Table 6 shows the ^{3}MLCT contributions for the corresponding

Table 6
Calculated metal-based charge transfer character (^{3}MLCT%), emitting energy (E_{T1}), transition dipole moment (μ_{S3}), ZFS parameters, radiative decay rate constants k_r and SOC matrix elements of the $T_1 \rightarrow S_0$ transitions for **1**–**3** at their respective T_1^{opt} optimized geometries obtained by the ADF2013.01 program package, along with the experimental value.

Complexes	^{3}MLCT (%)	E_{T_1} (eV)	μ_{S3} (Debye)	$k_{r,caled}$ (10^5 s^{-1})	ΔE_{1-2} (cm^{-1})	ΔE_{1-3} (cm^{-1})	Exp.[a] k_r (10^5 s^{-1})	$\langle S_0\|H_{SO}\|T_1\rangle$ (cm^{-1})
1	31.52	1.82	1.97	1.34	24.8	38.8	2.5	255
2	26.31	2.27	1.44	1.92	14.3	89.2		236
3	33.91	2.07	2.65	2.53	10.1	75.3		233

ΔE_{1-2} and ΔE_{1-3} parameters refer to the energy shifts between spin sublevels of T_1 excited state.
[a] Ref. [29].

excitations. It is notable that each of the complexes has a substantial ^{3}MLCT% contribution to T_1 state, especially for complex **3**, which renders more metal 5d(Ir) contribution to the occupied molecular orbitals, and hence greatly improving the SOC values.

Furthermore, strong SOC interactions can also account for the efficient ISC rate [53]. A qualitative description of the ISC rate can be performed as a function of the SOC matrix elements and energy separation between the singlet and triplet states [46,53–55]. Thus, the fast ISC rate will be achieved due to the large SOC constants coupled with the decreased singlet–triplet splitting energy. The calculated excitation energy levels of the three complexes at their respective optimized T_1 geometries are drawn in Fig. 5. As for **3**, owing to the largest transition dipole moment of S_3 excited state (Table 6) and the closest separation between S_3 and T_4, the fast ISC is expectable from the $S_3 \rightarrow T_4$, as is corroborated by $\langle T_4|H_{SO}|S_3\rangle$ matrix element, and then followed by a rapid internal conversion of $T_4 \rightarrow T_1$. This behavior leads to the significant contribution to the total ISC rate in a photoluminescence process for complex **3**, and thus a higher quantum yield will be achieved. A similar description also holds for complex **2**, which possesses relatively larger $\langle T_2|H_{SO}|S_3\rangle$ value and comparative energy gap between S_3 and T_2 states among the three complexes (Table 5 and Fig. 5), therefore, a fast ISC from the $S_3 \rightarrow T_2$ is expected, then relaxes to the light-emitting T_1 excited state. However, with respect to complex **1**, ISC process seems to be weaker due to the smaller $\langle T_m|H_{SO}|S_3\rangle$ matrix elements ($m = 1$–3) in Table 5, which corroborates the calculated result of k_r value as listed in Table 6. Moreover, higher energy of T_1 emitting state for the designed complexes can be observed (Table 6) with respect of complex **1**, which also contribute to the large k_r values for **2** and **3** to some extent according to Eq. (2).

Table 6 shows the theoretically calculated k_r values of T_1 excited state for the three complexes. For complex **1**, although the $k_{r,caled}$ is underestimated, the deviation is acceptable, and the values of

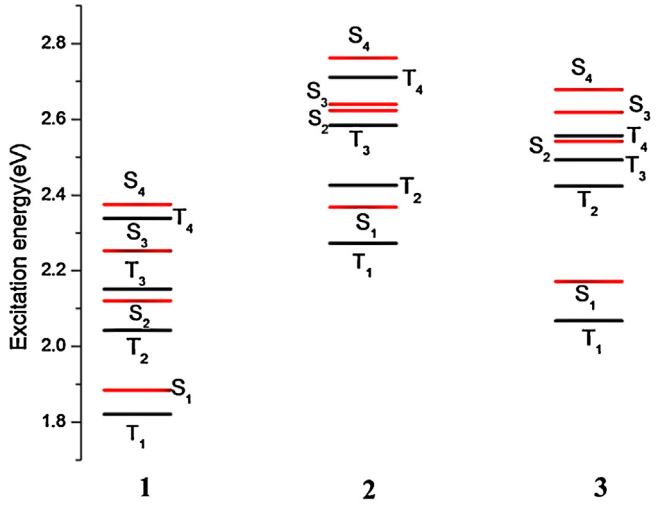

Fig. 5. Calculated excitation energy levels of **1**–**3** at their respective T_1 optimized geometries.

$k_{r,caled}$ reproduces the same order of magnitude of $k_{r,exptl}$ value, demonstrating the accuracy of the theoretical computations. It is easy to observe that the trend of k_r is predicted as follows: **3** > **2** > **1**, which confirms our previous inference. As discussed above, the relatively larger k_r values for the designed complexes **2** and **3** can be dependent on the dominant SOC effects, larger E_{T1} values and transition electric dipole moment (μ_{S3}).

Furthermore, the ZFS is another useful parameter in elucidating the performance of a phosphorescent organic-transition metal complex in OLED applications [7,50,56]. In general, the larger ΔE(ZFS) parameter, which is related to the greater ^{1,3}MLCT character in the corresponding excited states, can induce pronounced SOC and fast k_r [7,50]. Deduced from the ΔE(ZFS) parameters listed in Table 6, we noted that the ΔE_{1-3} parameters for the designed compounds are larger than that of **1**, which also provide an interpretation of the fact that the k_r values for these two compounds are larger than **1**.

Besides the effect of the k_r, k_{nr} is also crucial to determine the quantum yield of phosphorescence. Thus, it is necessary to provide insight into the k_{nr} of the three complexes. Previous literature [57–59] have demonstrated that the square of the SOC matrix element $\langle S_0|H_{SO}|T_1\rangle^2$ reflects the rate of the nonradiative quenching rate of the T_1 state to the S_0 state. Therefore, a smaller value of the $\langle S_0|H_{SO}|T_1\rangle$ is desirable, which would lead to a lower k_{nr} and then a higher quantum yield. By applying TD-DFT calculations with the use of perturbation theory, the value of $\langle S_0|H_{SO}|T_1\rangle$ can be determined and listed in Table 6. It is noted that the $\langle S_0|H_{SO}|T_1\rangle$ value for complex **3** (233 cm^{-1}) is smaller than that of **1** and **2** (255 and 236 cm^{-1}), which would result in a relatively lower k_{nr}. In a word, with the larger k_r and smaller k_{nr} values for complex **3**, we can draw a conclusion that it could have a relatively higher Φ_{PL} compared with the synthesized **1**. Therefore, complex **3** could become the potential highly efficient guanidinate-based emitting material.

Additionally, a high-performance OLED device is mainly dependent on the relative balance between hole and electron transportation and the charge injection abilities [49,60–62]. To roughly evaluate the hole injection and charge-transporting balance features, the vertical ionization potential (IP_v), hole reorganization energy (λ_h) as well as electron reorganization energy (λ_e) were also calculated for the studied complexes. The detailed results manifest that complex **3** has the smallest IP_v value (5.55 eV) relative to complex **1** and **2** (5.88 and 5.95 eV, respectively), and thus leads to a better hole injection ability. It is also noted that the energy differences between λ_h and λ_e for complexes **1** and **2** (0.01 and 0.02 eV respectively) are relatively smaller than those for **3** (0.04 eV), confirming their balanced charge transfer performance.

4. Conclusions

The features of the synthesized guanidinate-based iridium(III) complex **1** bearing the structure of $[(ppy)_2Ir\{(N^iPr)_2C(NPh_2)\}]$, have been thoroughly investigated by DFT/TD-DFT calculations including electronic structures, spectral properties, phosphorescence efficiency, and its performance in OLED device. Furthermore, two derivatives **2** and **3** have been designed based on **1** to explore

the effects of cyclometalated ligands on photophysical properties. In light of our results, the modification of main ligand from 2-phenylpyridine to phenylpyrazole and phenylimidazole can significantly destabilize the LUMO levels and thus, increase the HOMO–LUMO energy gaps for **2** and **3**. Besides, the absorption spectra of **2** and **3** are obviously blue-shifted and the enhanced intensity can be observed in the lower-energy region for **3**. The emission wavelength of **2** has a significant blue shift by 54 nm compared with **1**. Moreover, on closer inspection of the Φ_{PL}, the higher Φ_{PL} of **3** with relatively larger k_r and smaller k_{nr} compared to **1** can be ascribed to its larger SOC values, higher μ_{S3}, larger E_{T1} and smaller $<S_0|H_{SO}|T_1>^2$ value. Additionally, further analysis also indicate that **3** possesses an improved hole injection ability compared with **1**. Therefore, replacing the pyridyl functionality of ppy with diazole groups can have better photophysical properties than the synthesized **1**. To sum up, we predict that complex **3** can serve as a promising candidate for highly efficient guanidinate ligated iridium(III) phosphorescent material. This theoretical study provides a systematic elucidation of the relationship between $C\hat{N}$ ligands and photophysical properties of phosphorescent iridium(III) complexes. We hope this work can help to guide future design and synthesis of highly efficient phosphorescent OLED materials.

Acknowledgments

The authors gratefully acknowledge financial support from NSFC (21131001, 21273030, 21203019 and 21203020), SRFDP and RGC ERG Joint Research Program (20120043140001) and the Science and Technology Development Planning of Jilin Province (201201071 and 201201067).

Appendix A. Supplementary data

Supplementary data associated with this article can be found, in the online version, at http://dx.doi.org/10.1016/j.jmgm.2014.05.005.

References

[1] Y. Sun, N.C. Giebink, H. Kanno, B. Ma, M.E. Thompson, S.R. Forrest, Management of singlet and triplet excitons for efficient white organic light-emitting devices, Nature 440 (2006) 908–912.
[2] M.A. Baldo, D.F. O'Brien, Y. You, A. Shoustikov, S. Sibley, M.E. Thompson, S.R. Forrest, Highly efficient phosphorescent emission from organic electroluminescent devices, Nature 395 (1998) 151–154.
[3] Y. Zhang, L.L. Zhang, R.S. Wang, X.M. Pan, Theoretical study on the electronic structure and optical properties of carbazole-π-dimesitylborane as bipolar fluorophores for nondoped blue OLEDs, J. Mol. Graph. Model. 34 (2012) 46–56.
[4] G.M. Farinola, R. Ragni, Electroluminescent materials for white organic light emitting diodes, Chem. Soc. Rev. 40 (2011) 3467–3482.
[5] K.T. Kamtekar, A.P. Monkman, M.R. Bryce, Recent advances in white organic light-emitting materials and devices (WOLEDs), Adv. Mater. 22 (2010) 572–582.
[6] R. Jin, S. Tang, Theoretical study on optical and electronic properties of bipolar molecules with 1, 8-naphthalimide and triphenylamine moieties as organic light-emitting materials, J. Mol. Graph. Model. 42 (2013) 120–128.
[7] H. Yersin, W.J. Finkenzeller, in: H. Yersin (Ed.), Highly Efficient OLEDs with Phosphorescent Materials, Edition edn, Wiley-VCH, Weinheim, 2008, pp. 1–97.
[8] J. Wang, F.-Q. Bai, B.-H. Xia, H.-X. Zhang, Efficient blue-emitting Ir(III) complexes with phosphine carbanion-based ancillary ligand: a DFT study, J. Phys. Chem. A 115 (2011) 11689–11695.
[9] J.H. Seo, S.J. Lee, B.M. Seo, S.J. Moon, K.H. Lee, J.K. Park, S.S. Yoon, Y.K. Kim, White organic light-emitting diodes showing nearly 100% internal quantum efficiency, Org. Electron. 11 (2010) 1759–1766.
[10] A. M'Hamedi, A.S. Batsanov, M.A. Fox, M.R. Bryce, K. Abdullah, H.A. Al-Attar, A.P. Monkman, Dinuclear iridium(III) complexes of cyclometalated fluorenylpyridine ligands as phosphorescent dopants for efficient solution-processed OLEDs, J. Mater. Chem. 22 (2012) 13529–13540.
[11] S. Koseki, N.-o. Kamata, T. Asada, S. Yagi, H. Nakazumi, T. Matsushita, Spin–orbit coupling analyses of the geometrical effects on phosphorescence in Ir(ppy)3 and its derivatives, J. Phys. Chem. C 117 (2013) 5314–5327.
[12] S. Lamansky, P. Djurovich, D. Murphy, F. Abdel-Razzaq, R. Kwong, I. Tsyba, M. Bortz, B. Mui, R. Bau, M.E. Thompson, Synthesis and characterization of phosphorescent cyclometalated iridium complexes, Inorg. Chem. 40 (2001) 1704–1711.
[13] C.-H. Yang, M. Mauro, F. Polo, S. Watanabe, I. Muenster, R. Fröhlich, L. De Cola, Deep-blue-emitting heteroleptic Iridium(III) complexes suited for highly efficient phosphorescent OLEDs, Chem. Mater. 24 (2012) 3684–3695.
[14] Y. Tao, Q. Wang, C. Yang, C. Zhong, J. Qin, D. Ma, Multifunctional triphenylamine/oxadiazole hybrid as host and exciton-blocking material: high efficiency green phosphorescent OLEDs using easily available and common materials, Adv. Funct. Mater. 20 (2010) 2923–2929.
[15] Y. Kang, Y.-L. Chang, J.-S. Lu, S.-B. Ko, Y. Rao, M. Varlan, Z.-H. Lu, S. Wang, Highly efficient blue phosphorescent and electroluminescent Ir(III) compounds, J. Mater. Chem. C 1 (2013) 441–450.
[16] C. Adachi, R.C. Kwong, P. Djurovich, V. Adamovich, M.A. Baldo, M.E. Thompson, S.R. Forrest, Endothermic energy transfer: a mechanism for generating very efficient high-energy phosphorescent emission in organic materials, Appl. Phys. Lett. 79 (2001) 2082–2084.
[17] Q.L. Xu, C.C. Wang, T.Y. Li, M.Y. Teng, S. Zhang, Y.M. Jing, X. Yang, W.N. Li, C. Lin, Y.X. Zheng, J.L. Zuo, X.Z. You, Syntheses, photoluminescence, and electroluminescence of a series of iridium complexes with trifluoromethyl-substituted 2-phenylpyridine as the main ligands and tetraphenylimidodiphosphinate as the ancillary ligand, Inorg. Chem. 52 (2013) 4916–4925.
[18] Y. Kawamura, K. Goushi, J. Brooks, J.J. Brown, H. Sasabe, C. Adachi, 100% phosphorescence quantum efficiency of Ir(III) complexes in organic semiconductor films, Appl. Phys. Lett. 86 (2005) 071104.
[19] S.C. Lo, N.A.H. Male, J.P.J. Markham, S.W. Magennis, P.L. Burn, O.V. Salata, I.D.W. Samuel, Green phosphorescent dendrimer for light-emitting diodes, Adv. Mater. 14 (2002) 975–979.
[20] B.X. Mi, Z.Q. Gao, C.S. Lee, S.T. Lee, H.L. Kwong, N.B. Wong, Reduction of molecular aggregation and its application to the high-performance blue perylene-doped organic electroluminescent device, Appl. Phys. Lett. 75 (1999) 4055–4057.
[21] G. Chandra, A.D. Jenkins, M.F. Lappert, R.C. Srivastava, Amido-derivatives of metals and metalloids. Part X. Reactions of titanium(IV), zirconium(IV), and hafnium(IV) amides with unsaturated substrates, and some related experiments with amides of boron, silicon, germanium, and tin(IV), J. Chem. Soc. A (1970) 2550–2558.
[22] A.A. Trifonov, Guanidinate and amidopyridinate rare-earth complexes: Towards highly reactive alkyl and hydrido species, Coord. Chem. Rev. 254 (2010) 1327–1347.
[23] C. Jones, Bulky guanidinates for the stabilization of low oxidation state metallacycles, Coord. Chem. Rev. 254 (2010) 1273–1289.
[24] F.T. Edelmann, Chapter 3 advances in the coordination chemistry of amidinate and guanidinate ligands, Adv. Organomet. Chem. 57 (2008) 183–352.
[25] M.P. Coles, Application of neutral amidines and guanidines in coordination chemistry, Dalton Trans. (2006) 985–1001.
[26] P.J. Bailey, S. Pace, The coordination chemistry of guanidines and guanidinates, Coord. Chem. Rev. 214 (2001) 91–141.
[27] D. Elorriaga, F. Carrillo-Hermosilla, A. Antiñolo, I. López-Solera, R. Fernández-Galán, A. Serrano, E. Villaseñor, Synthesis, characterization and reactivity of new dinuclear guanidinate diimidoniobium complexes, Eur. J. Inorg. Chem. 2013 (2013) 2940–2946.
[28] X. Zhang, C. Wang, M. Xue, Y. Zhang, Y. Yao, Q. Shen, Synthesis and structure of samarium benzyl complex supported by bridged bis(guanidinate) ligand and its reactivity toward nitriles and phenyl isocyanate, J. Organomet. Chem. 716 (2012) 86–94.
[29] V.K. Rai, M. Nishiura, M. Takimoto, S. Zhao, Y. Liu, Z. Hou, Bis-cyclometalated iridium(III) complexes bearing ancillary guanidinate ligands. Synthesis, structure, and highly efficient electroluminescence, Inorg. Chem. 51 (2012) 822–835.
[30] V.K. Rai, M. Nishiura, M. Takimoto, Z. Hou, Guanidinate ligated iridium(III) complexes with various cyclometalated ligands: synthesis, structure, and highly efficient electrophosphorescent properties with a wide range of emission colours, J. Mater. Chem. C 1 (2013) 677–689.
[31] J.P. Perdew, K. Burke, M. Ernzerhof, Generalized gradient approximation made simple, Phys. Rev. Lett. 77 (1996) 3865–3868.
[32] E. Runge, E.K.U. Gross, Density-functional theory for time-dependent systems, Phys. Rev. Lett. 52 (1984) 997–1000.
[33] C. Adamo, V. Barone, Toward reliable density functional methods without adjustable parameters: the PBE0 model, J. Chem. Phys. 110 (1999) 6158–6170.
[34] J. Autschbach, T. Ziegler, S.J.A. van Gisbergen, E.J. Baerends, Chiroptical properties from time-dependent density functional theory. I. Circular dichroism spectra of organic molecules, J. Chem. Phys. 116 (2002) 6930–6940.
[35] K.L. Bak, P. Jorgensen, T. Helgaker, K. Ruud, H.J.A. Jensen, Gauge-origin independent multiconfigurational self-consistent-field theory for vibrational circular dichroism, J. Chem. Phys. 98 (1993) 8873–8887.
[36] T. Helgaker, P. Jorgensen, An electronic Hamiltonian for origin independent calculations of magnetic properties, J. Chem. Phys. 95 (1991) 2595–2601.
[37] J. Tomasi, B. Mennucci, R. Cammi, Quantum mechanical continuum solvation models, Chem. Rev. 105 (2005) 2999–3094.
[38] P.J. Hay, W.R. Wadt, Ab initio effective core potentials for molecular calculations. Potentials for K to Au including the outermost core orbitals, J. Chem. Phys. 82 (1985) 299–310.
[39] M.J. Frisch, G.W. Trucks, H.B. Schlegel, G.E. Scuseria, M.A. Robb, J.R. Cheeseman, G. Scalmani, V. Barone, B. Mennucci, G.A. Petersson, H. Nakatsuji, M. Caricato, X. Li, H.P. Hratchian, A.F. Izmaylov, J. Bloino, G. Zheng, J.L. Sonnenberg, M. Hada, M. Ehara, K. Toyota, R. Fukuda, J. Hasegawa, M. Ishida, T. Nakajima, Y. Honda, O. Kitao, H. Nakai, T. Vreven, J.A. Montgomery Jr., J.E. Peralta, F. Ogliaro, M.

Bearpark, J.J. Heyd, E. Brothers, K.N. Kudin, V.N. Staroverov, R. Kobayashi, J. Normand, K. Raghavachari, A. Rendell, J.C. Burant, S.S. Iyengar, J. Tomasi, M. Cossi, N. Rega, J.M.M. Millam, M. Klene, J.E.K. Knox, J.B.C. Cross, V. Bakken, C. Adamo, J. Jaramillo, R. Gomperts, R.E. Stratmann, O. Yazyev, A.J. Austin, R. Cammi, C. Pomelli, J.W. Ochterski, R.L. Martin, K. Morokuma, V.G. Zakrzewski, G.A. Voth, P. Salvador, J.J. Dannenberg, S. Dapprich, A.D. Daniels, O. Farkas, J.B. Foresman, J.V. Ortiz, J. Cioslowski, D.J. Fox, Gaussian 09, Revision A. 02, Gaussian, Inc., Wallingford CT, 2009.

[40] E. van Lenthe, E.J. Baerends, J.G. Snijders, Relativistic total energy using regular approximations, J. Chem. Phys. 101 (1994) 9783–9792.

[41] E.v. Lenthe, E.J. Baerends, J.G. Snijders, Relativistic regular two-component Hamiltonians, J. Chem. Phys. 99 (1993) 4597–4610.

[42] ADF 2013.01, SCM. Theoretical Chemistry Vrije Universiteit Amsterdam. The Netherlands; http://www.scm.com

[43] S.I. Gorelsky, AOMix: Program for Molecular Orbital Analysis, University of Ottawa, Ottawa, Ontario, Canada, 2007, http://www.sg-chem.net/ (accessed 12.04.11).

[44] N.M. O'Boyle, A.L. Tenderholt, K.M. Langner, cclib: A library for package-independent computational chemistry algorithms, J. Comput. Chem. 29 (2008) 839–845.

[45] Y. Liu, G. Gahungu, X. Sun, X. Qu, Z. Wu, Effects of N-substitution on phosphorescence efficiency and color tuning of a series of Ir(III) complexes with a phosphite tripod ligand: A DFT/TDDFT study, J. Phys. Chem. C 116 (2012) 26496–26506.

[46] Y. Liu, X. Sun, G. Gahungu, X. Qu, Y. Wang, Z. Wu, DFT/TDDFT investigation on the electronic structures and photophysical properties of phosphorescent Ir(III) complexes with conjugated/non-conjugated carbene ligands, J. Mater. Chem. C 1 (2013) 3700–3710.

[47] J. Su, X. Sun, G. Gahungu, X. Qu, Y. Liu, Z. Wu, Theoretical study on photophysical properties of cyclometalated cationic iridium(III) complexes containing dipyrido[3, 2-f:2′,3′-h]quinoxaline ligand, Synth. Met. 162 (2012) 1392–1400.

[48] A.B. Tamayo, B.D. Alleyne, P.I. Djurovich, S. Lamansky, I. Tsyba, N.N. Ho, R. Bau, M.E. Thompson, Synthesis and characterization of facial and meridional tris-cyclometalated Iridium(III) complexes, J. Am. Chem. Soc. 125 (2003) 7377–7380.

[49] Y. Liu, G. Gahungu, X. Sun, J. Su, X. Qu, Z. Wu, Theoretical study on the influence of ancillary and cyclometalated ligands on the electronic structures and optoelectronic properties of heteroleptic iridium(III) complexes, Dalton Trans. 41 (2012) 7595–7600.

[50] G.S.-M. Tong, C.-M. Che, Emissive or nonemissive? A theoretical analysis of the phosphorescence efficiencies of cyclometalated platinum(II) complexes, Chem. Eur. J. 15 (2009) 7225–7230.

[51] T. Matsushita, T. Asada, S. Koseki, Relativistic study on emission mechanism in Tris(2-phenylpyridine)iridium, J. Phys. Chem. C 111 (2007) 6897–6900.

[52] S. Haneder, E. Da Como, J. Feldmann, J.M. Lupton, C. Lennartz, P. Erk, E. Fuchs, O. Molt, I. Münster, C. Schildknecht, G. Wagenblast, Controlling the radiative rate of deep-blue electrophosphorescent organometallic complexes by singlet-triplet gap engineering, Adv. Mater. 20 (2008) 3325–3330.

[53] P.-T. Chou, Y. Chi, M.-W. Chung, C.-C. Lin, Harvesting luminescence via harnessing the photophysical properties of transition metal complexes, Coord. Chem. Rev. 255 (2011) 2653–2660.

[54] D.N. Kozhevnikov, V.N. Kozhevnikov, M.Z. Shafikov, A.M. Prokhorov, D.W. Bruce, J.A. Gareth Williams, Phosphorescence vs. fluorescence in cyclometalated Platinum(II) and Iridium(III) complexes of (Oligo)thienylpyridines, Inorg. Chem. 50 (2011) 3804–3810.

[55] C.-H. Yang, Y.-M. Cheng, Y. Chi, C.-J. Hsu, F.-C. Fang, K.-T. Wong, P.-T. Chou, C.-H. Chang, M.-H. Tsai, C.-C. Wu, Blue-emitting heteroleptic Iridium(III) complexes suitable for high-efficiency phosphorescent OLEDs, Angew. Chem. Int. Ed. 46 (2007) 2418–2421.

[56] Y. Wu, S.X. Wu, H.B. Li, Y. Geng, Z.M. Su, Forward molecular design for highly efficient OLED emitters: a theoretical analysis of photophysical properties of platinum(II) complexes with N-heterocyclic carbene ligands, Dalton Trans. 40 (2011) 4480–4490.

[57] A.R.G. Smith, M.J. Riley, P.L. Burn, I.R. Gentle, S.C. Lo, B.J. Powell, Effects of fluorination on Iridium(III) complex phosphorescence: magnetic circular dichroism and relativistic time-dependent density functional theory, Inorg. Chem. 51 (2012) 2821–2831.

[58] Q. Cao, J. Wang, Z.-S. Tian, Z.-F. Xie, F.-Q. Bai, Theoretical investigation on the photophysical properties of N-heterocyclic carbene iridium (III) complexes (fpmb)xIr(bptz)3 − x (x = 1–2), J. Comput. Chem. 33 (2012) 1038–1046.

[59] X. Li, B. Minaev, H. Ågren, H. Tian, Density functional theory study of photophysical properties of Iridium(III) complexes with phenylisoquinoline and phenylpyridine ligands, J. Phys. Chem. C 115 (2011) 20724–20731.

[60] R. Marcus, Electron transfer reactions in chemistry. Theory and experiment, Rev. Mod. Phys. 65 (1993) 599–610.

[61] N.S. Hush, Adiabatic rate processes at electrodes. I. Energy–charge relationships, J. Chem. Phys. 28 (1958) 962–972.

[62] R.A. Marcus, On the theory of oxidation-reduction reactions involving electron transfer, J. Chem. Phys. 24 (1956) 966–978.